Analysis of the Spatial Organization of Microtubule-associated Proteins

C. G. Jensen* and B. H. Smaill‡

*Department of Anatomy and ‡Department of Physiology, University of Auckland, School of Medicine, Private Bag, Auckland, New Zealand

Abstract. We have developed microdensitometer–computer correlation techniques to analyze the arrangement of microtubule arms and bridges (i.e., microtubule-associated proteins [MAPs]). A microdensitometer was used to scan immediately adjacent to the wall of longitudinally sectioned microtubules in positive transparency electron micrographs. Signal enhancement procedures were applied to the digitized densitometer output to produce a binary sequence representing the apparent axial spacing of MAP projections. These enhanced records were analyzed in two ways. (*a*) Autocorrelograms were formed for each record and correlogram peaks from a group of scans were pooled to construct a peak frequency histogram. (*b*) Cross-correlation was used to optimize the match between each enhanced record and templates predicted by different models of MAP organization. Seven symmetrical superlattices were considered as well as single axial repeats. The analyses were repeated with randomly generated records to establish confidence levels.

Using the above methods, we analyzed the intrarow bridges of the *Saccinobaculus* axostyle and the MAP2 projections associated with brain microtubules synthesized in vitro. We confirmed a strict 16-nm axial repeat for axostyle bridges. For 26 MAP2 records, the only significant match was to a 12-dimer superlattice model ($P < 0.02$). However, we also found some axial distances between MAP2 projections which were compatible with the additional spacings predicted by a 6-dimer superlattice. Therefore, we propose that MAP2 projections are arranged in a "saturated 12-dimer, unsaturated 6-dimer" superlattice, which may be characteristic of a wide variety of MAPs.

PROJECTIONS from the walls of microtubules are seen in electron micrographs as side-arms in isolated microtubules and as bridges between microtubules or microtubules and other organelles. The bridges are thought to mediate interactions of microtubules with each other or with other cellular organelles. They may play a skeletal role in maintaining the order of microtubule arrays (8, 35) or binding to actin (31). They are important in the function of motile organelles such as cilia and flagella (29, 41), flagellate axostyles (26, 42), and possibly the mitotic spindle (11, 15, 25). They may also play a role in the movement of organelles in a variety of cells, including nerves (9, 13), secretory cells (33, 36), melanophores (28), and protozoans (37).

Microtubule arms and bridges appear to be the morphological correlates of the group of high molecular weight polypeptides referred to collectively as microtubule-associated proteins (MAPs)[1] (reviewed in reference 3). For example, microtubules assembled in the presence of MAPs are decorated with fine filamentous projections, while those assembled in the absence of MAPs are smooth walled (4, 19, 27, 36, 40). In addition, the projections on microtubules assembled in the presence of the 300,000-mol-wt MAP2 are considerably longer than those associated with microtubules assembled in the presence of the 58,000–65,000-mol-wt tau (44).

Vallee (38) and co-workers (39) find that ~90% of the brain MAP2 molecule (the projection domain) forms the projection, while the remaining 10% (the assembly-promoting domain) is associated with the microtubule wall. The base of the projection appears to be structured to allow some flexibility (38, 40, 43). In thin sections, MAP2 projections extend 15–40 nm from the microtubule wall (19, 27, 40, 44).

Because of the probable importance of MAPs in microtubule assembly and function, there has been much interest in determining their precise arrangement on the microtubule surface. The most clearly understood arrangements are those of the various links associated with cilia and flagella (29, 41). The arrangement of arms and bridges associated with other microtubules is not immediately apparent. A number of studies have suggested the presence of strictly periodic binding sites along the microtubule wall (14, 19, 26, 27, 42); it has been argued that projections may randomly occupy these periodic sites (25, 40). Conversely, Amos (1–3) has suggested that the MAPs associated with brain microtubules composed of 13 protofilaments are regularly spaced along a superhelix on the surface of the microtubule such that the

1. *Abbreviation used in this paper*: MAP, microtubule-associated protein.

MAP projections are radially symmetric. These superlattices repeat after 13 attachment sites are traversed and thus may be characterized in terms of the number of tubulin dimers between MAP projections along a single protofilament. After considering different possible symmetrical superlattices, Amos concluded that one which repeats after 12 dimers was most consistent with electron microscopic images.

Previous investigators have attempted to determine the arrangement of MAPs through use of optical diffraction (1, 25), lateral image translation of electron micrograph transparencies (14, 19), measurement from electron micrographs (2, 25, 27), and visual enhancement by labeling with antibodies to MAPs (12, 34). The difficulties encountered in such techniques include the absence in electron micrographs of the long, discrete stretches of microtubules required for optical diffraction, difficulties in identifying arms and bridges, the fact that the projections are often tilted, and uncertainties in magnification resulting from inaccurate calibration of the electron microscope or shrinkage of specimens during preparation for electron microscopy.

In an attempt to better characterize the precise arrangement of MAP projections, we have developed a quantitative method which minimizes the difficulties mentioned above. Electron micrographs are scanned with a microdensitometer and the axial spacing of the projections is analyzed using auto- and cross-correlation techniques. We have found the technique to be particularly effective in analyzing the MAP2 projections of reconstituted brain microtubules and the intrarow bridges of the *Saccinobaculus* axostyle. The method should be equally useful in determining the arrangement of arms and bridges associated with microtubules from other sources and may find useful applications in related structural studies. Preliminary stages in the development of the technique have been reported elsewhere (10, 16–18, 32).

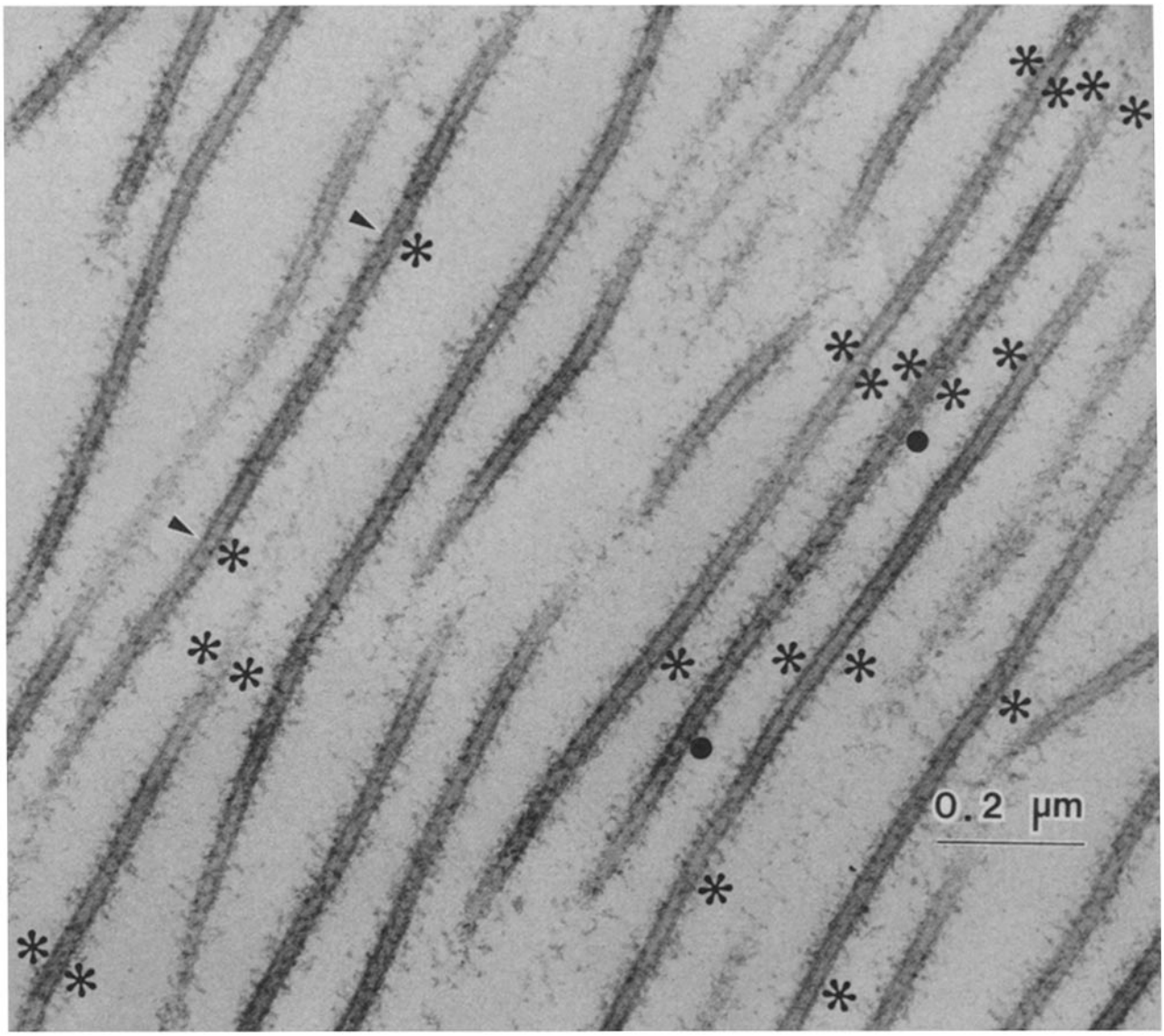

Figure 1. Electron micrograph of thin-sectioned microtubules synthesized in vitro and saturated with MAP2. Asterisks, arrowheads, and dots delineate 13 of the 26 areas which were analyzed in this study. Micrograph from H. Kim.

Materials and Methods

Data Acquisition and Enhancement

The material used for analysis was from thin sections of reconstituted calf brain microtubules saturated with MAP2, as described by Kim et al. (19). From three electron micrograph negatives with original magnifications of 25,100, we chose 26 different areas containing straight stretches of microtubules longer than 200 nm, with MAP2 projections that could be visually identified (Fig. 1). Positive transparencies of these areas were printed at final magnifications of 125,500, mounted on glass slides, and opaque tape was used to mask out the wall of each microtubule, leaving the MAP projections extending beyond the mask. We also prepared one transparency of the intrarow microtubule links from the *Saccinobaculus* axostyle (as in Fig. 5 *b* from reference 41).

The area adjacent to each masked microtubule segment (Fig. 2 *a*) was scanned with a purpose-built microdensitometer interfaced to a PDP 8/e or PDP 11/23 computer (10). A stepping motor controlled by the computer moved the transparency so that the fixed beam of the densitometer, which was directed normal to the transparency, traced a straight line parallel to the microtubule. To minimize the effect of projection tilt, scans were as close to the mask as possible. The slit size of the densitometer was 50 × 300 μm, with the long axis oriented perpendicular to the edge of the mask. The computer was programmed to advance the transparency in uniform increments, and for each step the densitometer output was digitized, averaged over the step increment, and stored (Fig. 2 *b*). Taking into account magnification of the micrographs, each step represented an actual distance of 0.8 nm along the microtubule.

All further analyses were carried out with a PDP 11/23 computer. To improve the signal-to-noise ratio of the digitized densitometer record, a low-pass recursive filter (23) was used to attenuate rapid density variations; baseline drift in the densitometer record resulting from spatial variation of contrast in the micrograph was removed with a piecewise linear correction algorithm; and the filtered densitometer record was converted to a binary data sequence consisting of values of zero or one (see Fig. 2, *a–e*). Points in the sequence with a value of one are referred to as peaks. These enhancement methods were tested on the MAP2 and *Saccinobaculus* densitometer records used in this study. For each area scanned, we visually identified all microtubule projections (without referring to the densitometer record), and then compared their location with the sequence of peaks in the enhanced densitometer record obtained from that area. Visual identification of all projections was facilitated by viewing positive transparency micrographs with a light box. For all the areas compared in this way, the number of projections identified by eye did not differ by more than 4% from the number of projections at corresponding positions in the associated enhanced densitometer record (compare Fig. 2 *a* with Fig. 2 *e* and Fig. 10 *a* with Fig. 10 *c*).

Models of MAP Organization

In this study, the arrangement of MAP projections was determined by serial densitometer measurements in a narrow window parallel to the edge of the microtubule. To compare these data with proposed models of MAP organization, we have set up a mathematical formulation which predicts the sequence of projections that would be expected within the scanning window for any symmetrical superlattice. Each superlattice is specified by the pitch of the helix and the number of protofilaments between adjacent MAP attachment sites (Fig. 3, *a–c*). The predicted orthographic projection of the MAPs can be determined in any viewing plane parallel to the longitudinal axis of the microtubule; for this purpose it was assumed that the model projections are normal to the microtubule (Fig. 3 *d*). The predicted axial spacing of MAPs is obtained by scoring projections which cross a line representing the position of the densitometer window (Fig. 3 *d*). For each model, three or four discrete patterns of MAP projections are observed as the distance between the scanning window and the microtubule is varied (compare Fig. 4 *a* with 4 *b*).

With axial rotation of the microtubule model, the orthographic projections of MAPs vary as they are obscured by the boundaries of the microtubule. Because of the repetitive structure of the symmetrical superlattices, the patterns of projections are, in fact, relatively invariant and often appear simply to have been translated along the axis of the microtubule. For the symmetrical superlattice models used in the present study, only two different patterns of axial spacing are observed during 24 sequential 15° rotations. For each model, we have called the more frequently occurring pattern 1

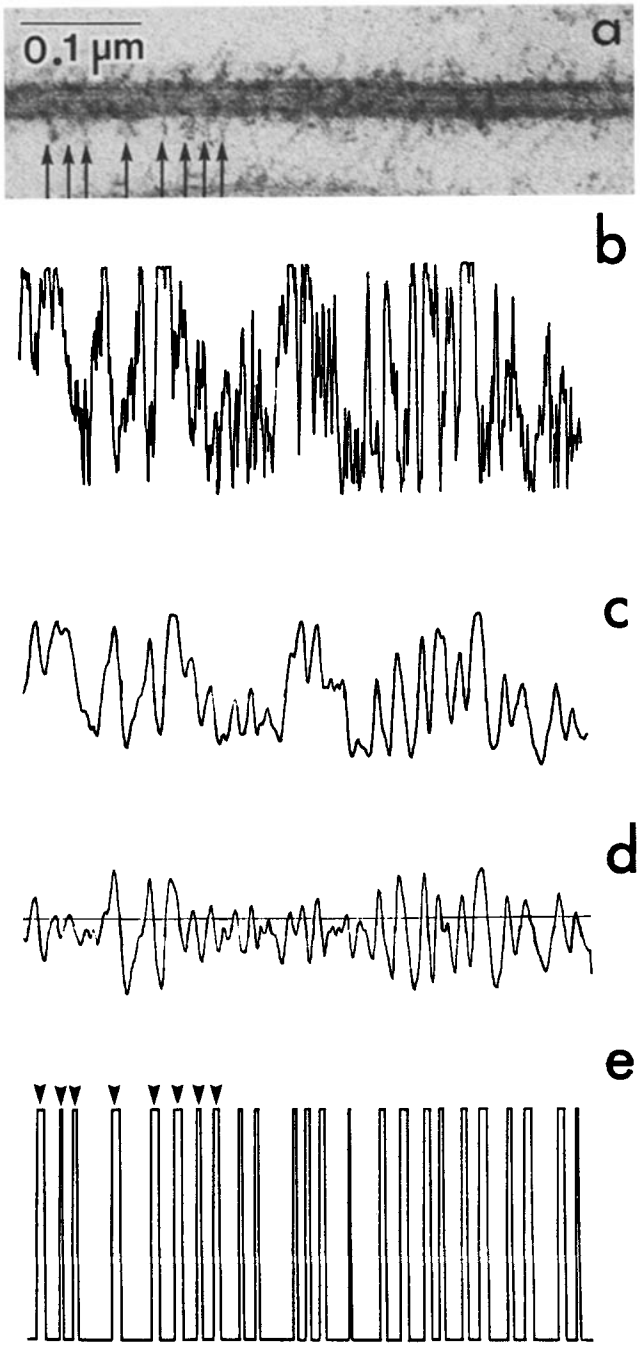

Figure 2. Data acquisition and enhancement techniques. The procedures used are illustrated for a scan of the region marked by arrowheads in Fig. 1. (*a*) The region scanned. Whereas we found individual MAP2 projections easy to identify from a positive transparency, they are more difficult to resolve in an electron micrograph such as this. However, the projections indicated by arrows on the left side of the microtubule can be identified and the corresponding peaks followed through the data enhancement steps in *b–e*. (*b*) Densitometer record obtained from *a*. (*c*) Effect of smoothing *b* with a two-pole recursive low-pass filter. (*d*) Result of applying base line correction to *c*. (*e*) Resultant binary sequence obtained from *d* by setting a threshold at 0.5 of its root mean square value (see horizontal line in *d*). Subthreshold densities were set to zero, while those above threshold were set to one. The latter points are referred to as peaks.

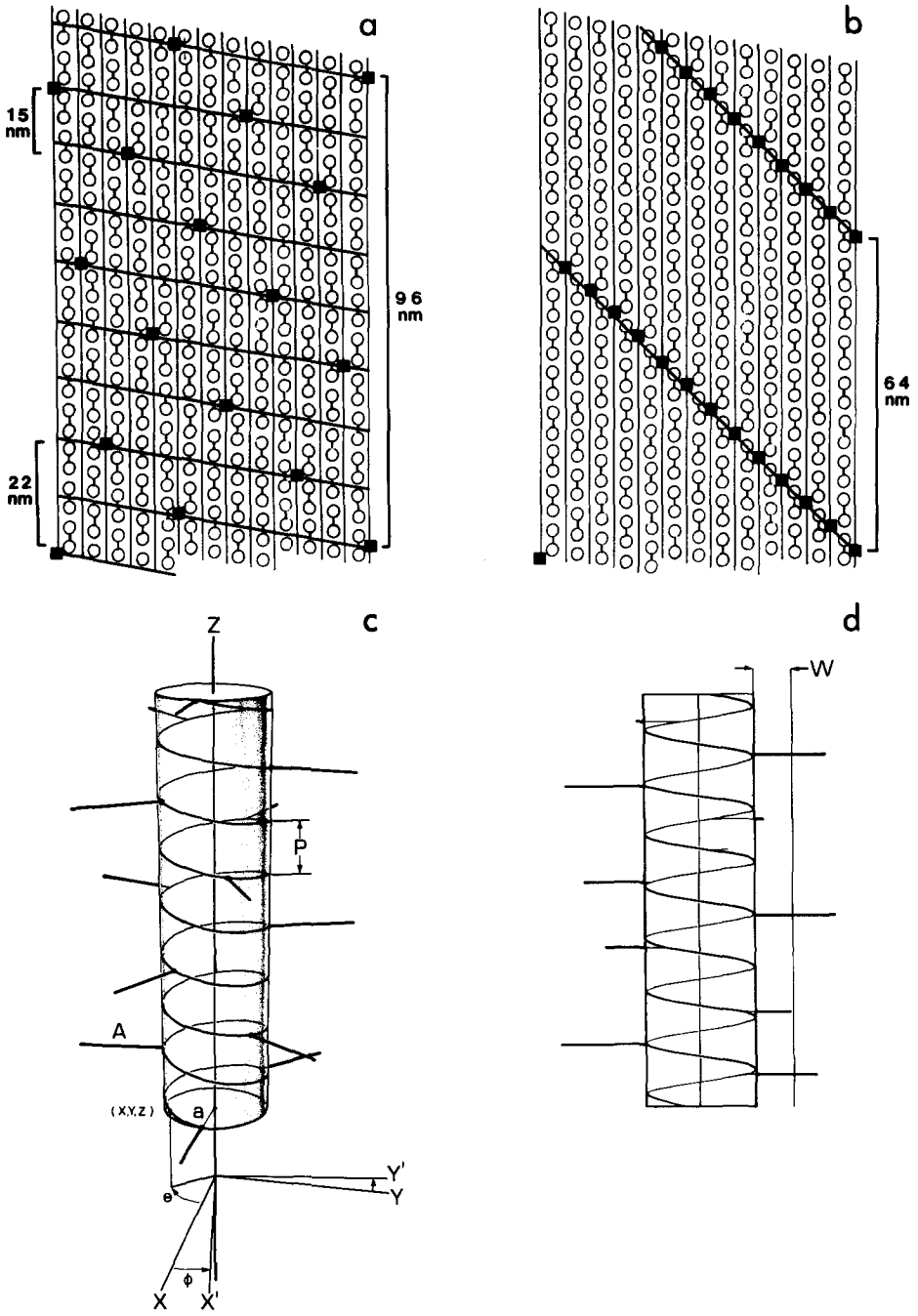

Figure 3. Symmetrical superlattice models of MAP arrangement. (*a* and *b*) Opened-out views of superlattices (1). The squares represent the sites of MAP projections which occur at regular intervals along the superhelix. Lines between the squares indicate the pitch of the superhelix. The characteristics of 14 superlattices are presented in Table I. (*a*) 12-dimer superlattice. (*b*) 8-dimer superlattice. (*c*) Three-dimensional representation of the 12-dimer model. *a*, radius of microtubule; *A*, length of sidearms; *p*, pitch of superhelix; (X,Y,Z), coordinates of any point on the superhelix; Θ, axial rotation of point (x,y,z) as it moves along the superhelix. The viewing coordinate system (X',Y',Z) is rotated about the Z-axis through the angle φ with respect to the microtubule. Although the helices in *a–d* and Table I are depicted as left-handed, an alternative right-handed helix also passes through all attachment sites. (*d*) Orthographic projection in the Y'-Z viewing plane of the microtubule model represented in *c*. The scanning window is represented by the parallel line situated a distance W (in this case, 9 nm) from the edge of the microtubule.

(Fig. 4, *a* and *b*, upper diagrams) and the less frequently occurring 2 (Fig. 4, *a* and *b*, lower diagrams).

Therefore, for symmetrical superlattice models of MAP organization the spacing of projections within a scanning window parallel to the microtubule axis will be determined by the following: the pitch of the superhelix; the number of protofilaments between adjacent MAP attachment sites; the distance of the scanning window from the edge of the microtubule; the orientation of the microtubule with respect to the viewing plane; the length of projections; and the radius of the microtubule. The variables used for the superlattice models are presented in Table I. The microtubule radius and the length of projections were fixed at the generally accepted values of 12 and 20 nm, respectively (2).

Autocorrelation

Autocorrelation was used to reveal repetitive structure within the experimental data. Autocorrelograms of unenhanced or enhanced data were formed by correlating the digitized densitometer record with a shifted template consisting of the first half of the record. Hence, this was not a complete "circular" autocorrelation. The template was translated one step at a time with respect to the data and for each shift the sum of the products of coincident samples was formed (23). Repetition of structure within the data generated peaks in the autocorrelogram at translations corresponding to the underlying periodicity. Autocorrelograms were scaled to give a maximum value of one when there was no shift between template and data.

Cross-Correlation

Cross-correlation was used to determine the correspondence between the data and models of MAP organization. Complete densitometer records were correlated with templates that were twice the record length and consisted of the binary sequences predicted by various models of MAP organization (see Fig. 4). These included some of the helical models specified in Table I, as well as models with a single axial repeat. For each model, the match between the data and the predictive template was optimized using a simple parameter adjustment scheme. The densitometer record was scaled in 1%

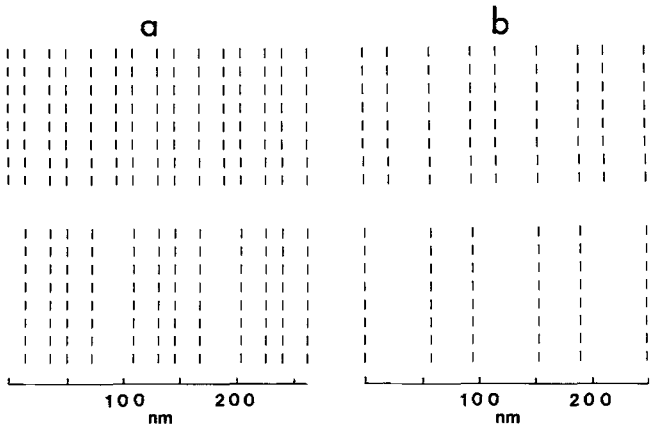

Figure 4. Changes in the orthographic projection of MAPs produced by rotating the microtubule about the Z-axis and varying the distance of the scanning window from the edge of the microtubule. Dashed lines indicate the axial positions of projections in the scanning window predicted by the 12-dimer model. (*a*) Scanning window 1 nm from edge of microtubule. (*Top*) Rotation pattern 1; axial spacings = 15 and 22 nm. (*Bottom*) Rotation pattern 2; axial spacings = 15, 22 and 37 nm. (*b*) Scanning window 14 nm from edge of microtubule. (*Top*) Rotation pattern 1; axial spacings = 22 and 37 nm. (*Bottom*) Rotation pattern 2; axial spacings = 37 and 59 nm.

steps between 90 and 110% of nominal length, a set of 21 cross-correlograms was formed and the combination of scaling and template translation which gave the maximum correlation was selected. For the helical models, this process was performed twice for each densitometer record, using as templates the two different axial rotations of the model which gave MAP distribution patterns 1 and 2.

The correspondence between enhanced data and a predictive template was quantified using the correlation index, $N_{1,2}^2/N_1N_2$; where N_1 is the number of peaks in the enhanced data sequence, N_2 is the number of projections in the template, and $N_{1,2}$ is the number of times template projections and data peaks coincide. It was necessary to account for tilting of sidearms (refer to Fig. 2 *a*) and variability of peak widths in the enhanced data sequences. Thus, a match was scored when the center of a data peak fell within a predetermined distance from the center of a template projection. The match tolerance of ±3.5 nm chosen for these studies slightly exceeded the normally observed MAP projection width of ~6 nm (27) and accommodated some variation in the orientation of projections.

It was necessary to establish whether an observed match between experimental data and template could have occurred by chance. To determine confidence levels, the cross-correlation analysis was repeated using randomly generated binary sequences. A random number generator was programmed to produce sequences with a range of peak widths comparable to the enhanced data (i.e., 4–7 nm); sequence lengths and mean spacing between peaks were within the range observed for the densitometer records. The random records were matched to predictive templates for each of the models studied, using a scaling of 90–100% and a ±3.5-nm match tolerance, and the best-fit correlation indices were evaluated (i.e., the same procedures as used for experimental data). Distributions of the resultant correlation indices were constructed for predetermined combinations of sequence length and mean peak spacing, using 50 different random records for each combination. In all cases, the best-fit correlation indices were normally distributed.

Confidence limits for the match between random binary sequences with a mean spacing between peaks of 22 nm and a 12-dimer template are presented in Fig. 5 *a*. As a datum spacing, 22 nm was chosen arbitrarily from average values for experimental data ranging from ~14 to 23 nm. Fig. 5 *a* demonstrates that a high correlation index is more likely to occur by chance in short records. For other models, the relationship between confidence levels and record length was similar.

Variation of the mean spacing between data peaks produced a small shift in the confidence levels for the best-fit correlation indices, which was similar at all record lengths. Therefore, it was necessary to account for this variation. The correction curve for a 12-dimer template is given in Fig. 5 *b*. The corrected best-fit correlation indices were then plotted as a function of record length, with the appropriate confidence limits for a mean spacing between data peaks of 22 nm superimposed on the graph (see Fig. 9). The standard normal deviate $(X - \mu)/\sigma$ was obtained for each corrected correlation index X; the mean μ and the standard deviation σ were evaluated from the confidence limits at the corresponding record length (see Fig. 5 *a*). The deviates were then averaged to obtain an estimate of the mean confidence level for a complete set of records obtained from the same material.

Results

Autocorrelation Analysis

It was difficult to resolve peaks in autocorrelograms constructed from unenhanced data (Fig. 6 *a*), but the use of enhanced data reduced this problem (Fig. 6, *b* and *c*). However,

Table I. Characteristics of Possible Symmetrical Superlattices for MAP Organization

Repeat Length		Pitch of superhelix	Protofilaments between MAPs along superhelix	Designated distance of scanning window from microtubule*	Basic axial spacings between MAP projections		Relative frequency of occurrence of pattern I
dimers	*nm*	*nm*	*n*	*nm*	1‡ *(nm)*	2‡ *(nm)*	%
3	24	12.0	2	9.0	2,9,11	2,11,13	54.2
4	32	4.57	7	9.0	5,17	5,22	54.2
5	40	40.0	1	9.0	3,31	3,34	54.2
6	48	12.0	4	9.0	11,26	11,15	70.8
7	56	14.0	4	9.0	13,17	13,30	54.2
8	64	64.0	1	9.0	5,49	5,54	54.2
9	72	12.0	6	1.0	11,28	11,39	70.8
10	80	40.0	2	9.0	6,31,37	6,37	54.2
11	88	29.33	3	9.0	7,27	27,34	54.2
12	96	12.0	8	1.0	15,22	15,22,37	70.8
14§	112	22.4	5	9.0	26,43	17,26,43	70.8
15	120	40.0	3	9.0	9,37	37,46	54.2
16	128	64.0	2	1.0	10,49	10,49,59	70.8
17	136	22.67	6	1.0	21,52	21,73	70.8

* The distance of the scanning window from the edge of the microtubule was set to give axial spacings between model projections which most closely approximated those observed in electron micrographs of MAP2.

‡ 1 and 2 represent the two possible patterns of axial spacings between MAP projections, where 1 is the more frequently occurring pattern.

§ For 13 protofilament microtubules there is no symmetrical superlattice which repeats after 13 dimers.

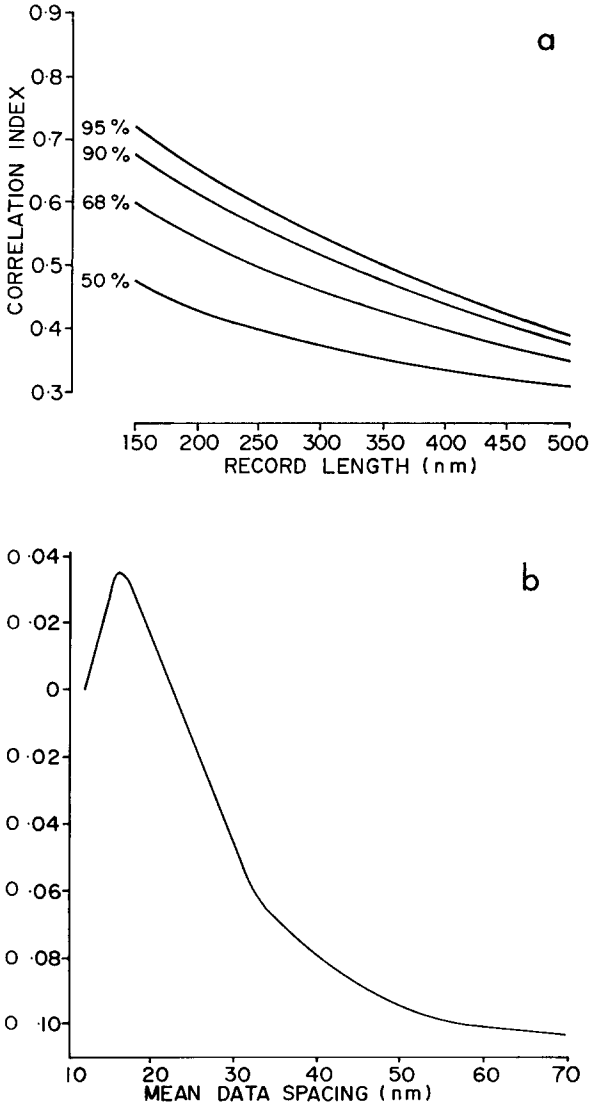

Figure 5. Features of the random distributions used to assess the significance of cross-correlation analysis for the 12-dimer model. (*a*) Confidence levels for the best-fit correspondence between the 12-dimer model and enhanced densitometer data with a 22-nm datum spacing, presented as a function of record length. (*b*) Corrections to correlation index for the 12-dimer model to adjust for deviations from a 22-nm mean data spacing.

for the relatively short records studied here, it was not possible to obtain objective information from a single autocorrelogram. For example, autocorrelograms constructed from some of the randomly generated records exhibited discrete peaks comparable to the experimental data (Fig. 6 *d*). Also,

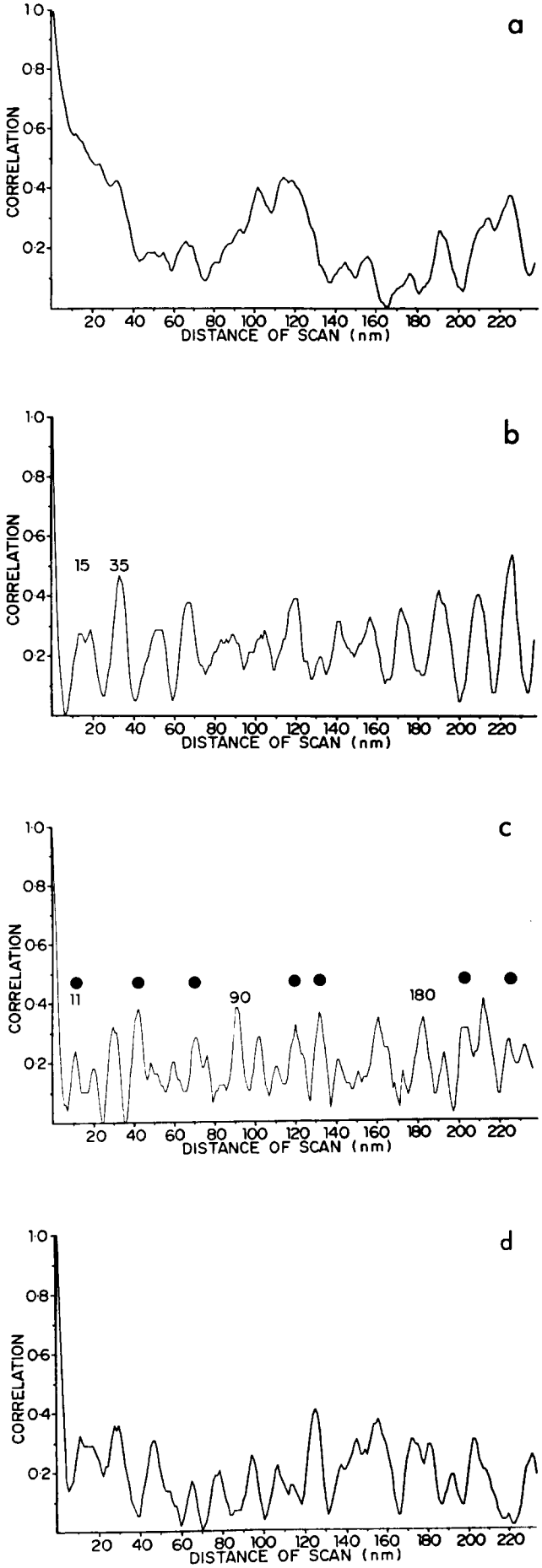

Figure 6. Autocorrelograms derived from densitometer records. (*a*) Autocorrelogram of unenhanced densitometer data in Fig. 2 *b*. (*b*) Autocorrelogram of enhanced densitometer data in Fig. 2 *e*. The peaks representing the basic spacings of a 12-dimer model are indicated. (*c*) Autocorrelogram of enhanced densitometer data derived from the area delineated by dots in Fig. 1. The peaks compatible with a 6-dimer, but not a 12-dimer superlattice are indicated by dots. (*d*) Selected autocorrelogram of a randomly generated binary record. The record was generated as described in the Materials and Methods: cross-correlation section and was one of those used to construct Fig. 5 *a*. The correlation index between the record and a 12-dimer model template = 0.277.

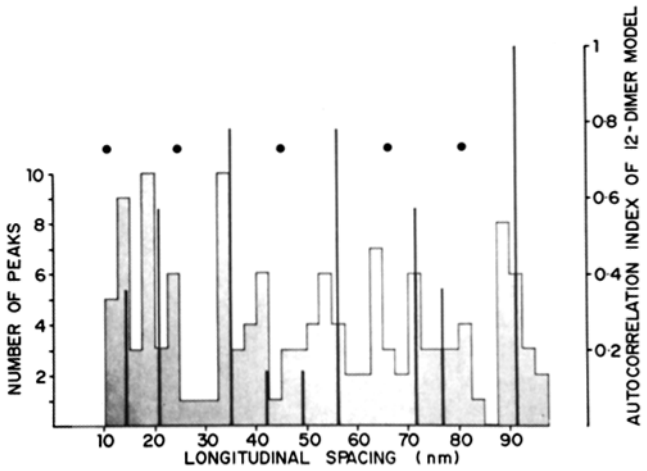

Figure 7. Autocorrelogram peak frequency histogram derived from 26 MAP2 densitometer records. Shaded areas indicate the number of peaks at each axial spacing (refer left-hand ordinate). Vertical lines indicate the spacing, scaled downward by 4%, and relative magnitude (refer right-hand ordinate) of peaks from a mean autocorrelogram of the 12-dimer superlattice model. For each model, mean autocorrelograms were constructed by averaging individual autocorrelograms derived from 24 sequential 15° axial rotations of the model (assuming that all rotations were equally probable). The dots indicate additional spacings predicted by a 6-dimer superlattice model, also scaled downward by 4%.

in autocorrelograms obtained from a shortened, enhanced densitometer record, the magnitude of peaks at the lower order spacings was greater in the truncated record than in the original.

To overcome these problems, we constructed an autocorrelogram peak frequency histogram, using clearly identifiable peaks in autocorrelograms from the 26 enhanced MAP2 files (Fig. 7). The histogram indicates the existence of a common, ordered structure within the densitometer records. The spacing of major peaks is not completely regular, and hence not consistent with a single axial repeat. On the other hand, a strong peak is seen in the histogram at 89–94 nm, suggesting that the underlying structure is repeated at this interval. Also, the pattern of spacing between peaks in the interval 0–92 nm was duplicated in the interval 92–184 nm (not shown).

The autocorrelogram peak frequency histogram was compared with a predictive mean autocorrelogram for each of the helical models described in Table 1. In Fig. 7, the mean autocorrelogram for the 12-dimer model is superimposed on the histogram. We scaled the predictive autocorrelogram spacings downward by 4% so that the 96-nm 12-dimer repeat length of the model coincided with the 92-nm peak consistently observed in the data. There is a considerable degree of correspondence between the spacing of peaks in this adjusted predictive autocorrelogram and those represented in the peak histogram. However, neither the consistently observed peak at 65 nm, nor the possible peaks at 11, 25, and 82 nm (indicated by black circles in Fig. 7) are predicted by the 12-dimer model. Peaks at these intervals were seen in 11 of the 26 MAP2 autocorrelograms used in the present study (Fig. 6 *c*).

Cross-Correlation Analysis

Cross-correlation analysis was applied to the 26 densitometer records of MAP2-decorated microtubules. The best fit between a typical enhanced record and the 12-dimer model is shown in Fig. 8. For 65% of the records, the translation which gave the optimal match was the same for both unenhanced and enhanced records. In Fig. 9, the corrected best-fit correlation indices for the 26 MAP2 records and the 12-dimer model are presented as a function of record length and compared with associated confidence limits. The correlation indices for each of the 26 records lie above the 50% confidence limit and in 17 cases exceed the 90% level. In Table II, the results of cross-correlation analysis are compared for the seven models of symmetrical superlattices with which the records were most compatible. The results for 24 and 32 nm axial repeats are also presented. The 12-dimer model provides a significantly better match to the enhanced densitometer records than do the other models. On the basis of the uncorrected correlation index, the 12-dimer model gives the best fit in 16 of the 26 records, compared with five for the next-best fit, the 7-dimer model. When the correlation indices are corrected for variation in mean spacing between data peaks, the overall mean confidence level for the match between the pooled 26 MAP2 files and the 12-dimer model is 98.2% ($P < 0.02$). The next best matches (i.e., the 17-dimer and the 24-nm axial repeat models with mean confidence levels of 81.9 and 85.9%, respectively) are not significant at the $P \leq 0.1$ level.

We have also used our cross-correlation technique to analyze the intrarow microtubule links from the *Saccinobaculus* axostyle, which have been reported to exhibit a 16-nm periodicity (26, 42). Although the unenhanced densitometer records are difficult to interpret, the enhanced data correlate perfectly with a 16-nm periodic template (Fig. 10, *a–d*).

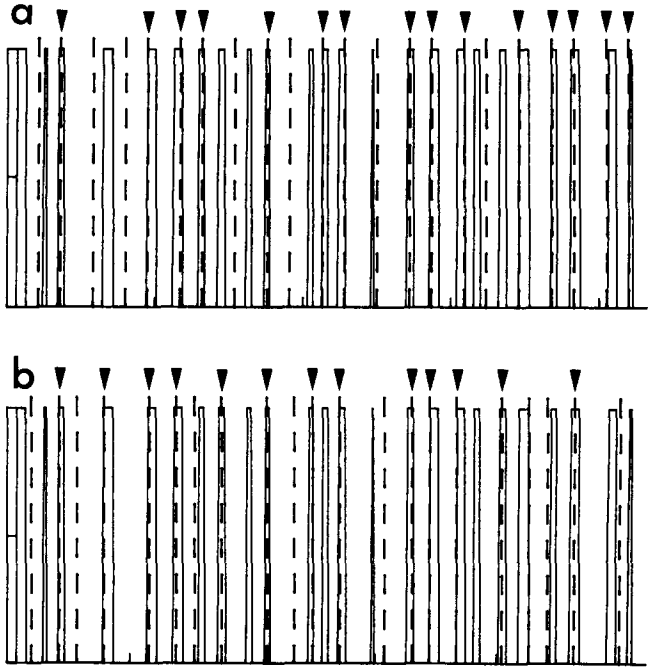

Figure 8. The best-fit correspondence between the enhanced densitometer record illustrated in Fig. 2 *e* and the 12-dimer model (dashed lines). Scanning window 1 nm from edge of microtubule. Arrowheads indicate matches between data and model. (*a*) Rotation pattern 1, correlation index = 0.426. Original data length scaled at 109% for best match. (*b*) Rotation pattern 2, correlation index = 0.335. Original data length scaled at 91% for best match.

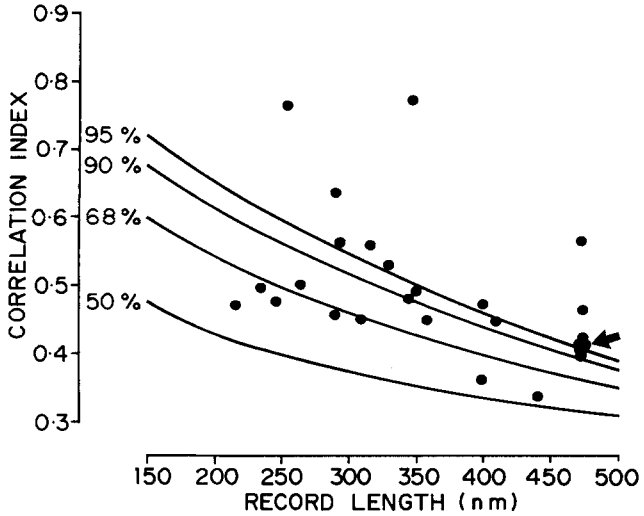

Figure 9. Correlation indices for the 26 enhanced MAP2 densitometer records and the 12-dimer model. The correlation indices have been corrected for variation in mean spacing between data peaks and are compared with the confidence levels for the 12-dimer model illustrated in Fig. 5 *a*. Arrow indicates the correlation index for the data presented in Figs. 2 and 8.

Discussion

We have developed quantitative methods for analyzing the spatial organization of projections associated with microtubules in electron micrographs. Using these techniques, we have demonstrated that the arrangement of MAP2 associated with brain microtubules is significantly more consistent with a 12-dimer symmetrical superlattice than with a random arrangement, with other symmetrical superlattices, or with models having a single axial repeat. Our methods overcome many of the problems encountered in previous attempts to analyze the axial spacing of microtubule projections (1, 14, 19, 25, 27, 40). For example, our technique can be applied to short records, as opposed to the long scans required for optical diffraction or Fourier analysis. Also, they overcome the subjectivity of visual identification and measurement of microtubule projections from micrographs. The cross-correlation analysis provides a means of testing various possible arrangements of projections and, within realistic limits, takes into account uncertainties in magnification, variations in orientation of microtubules, and tilting of projections. We are currently using the technique to analyze the arms and bridges associated with a variety of microtubules. The method should be equally useful for analyzing other regularly arranged structures from micrographs.

Table II. Correspondence of Enhanced MAP2 Densitometer Records to Model Templates (n = 26)

Model used as template*	Number of cases in which model is the best match to uncorrected data	Overall mean confidence level for corrected data
		%
6-dimer	0	6.8
7-dimer	5	71.9
9-dimer	1	46.8
12-dimer	16	98.2
14-dimer	2	79.4
15-dimer	2	65.9
17-dimer	0	81.9
24-nm repeat	0	85.9
32-nm repeat	0	64.8

* Models for other dimer repeats were not included in the analysis, as the predicted spacings were incompatible with the morphological data (see Fig. 3 *b* and Table I).

Data Enhancement

The use of data enhancement to produce a binary sequence is central to our technique for several reasons. (*a*) It is possible to identify discrete spectral peaks in autocorrelograms of enhanced records that are not resolved in autocorrelograms of unenhanced data (Fig. 6, *a* and *b*). (*b*) Enhancement yields a standardized data sequence, enabling objective evaluation of the match between microdensitometer data and model-derived templates. (*c*) It is possible to generate random bi-

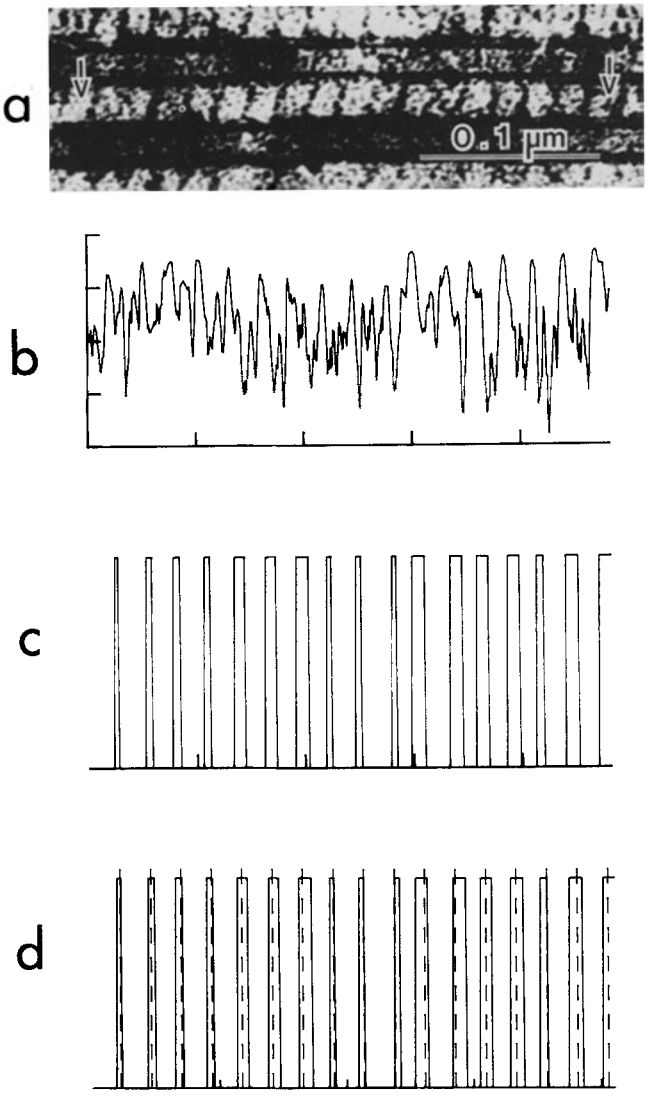

Figure 10. Results of cross-correlation analysis of the intrarow links of the *Saccinobaculus* axostyle. (*a*) The area scanned is delineated by arrows. (*b*) Unenhanced densitometer record obtained from *a*. (*c*) Enhanced densitometer record obtained from *b*. (*d*) Best-fit correspondence between enhanced densitometer record in *c* and a 16-nm axial repeat. Correlation index = 1.0.

nary records with peak widths, mean spacings, and record lengths similar to the enhanced data, allowing the significance of a particular match to be determined.

It could be argued that the data enhancement methods have introduced artifacts, some peaks being wrongly included in the processed densitometer record, and others incorrectly omitted. However, we are confident that the spatial information contained in the unenhanced data is preserved in the enhanced binary data sequence because (*a*) there is a good correspondence between projections identified visually in the original micrographs and peaks in the enhanced densitometer record (compare Fig. 10 *a* with Fig. 10 *c*), and (*b*) the translation giving the optimal match to a model-derived template is similar for unenhanced and enhanced records.

Correlation Analysis

The advantage of autocorrelation analysis is that it provides unbiased information on the axial spacings of MAP projections. However, for short record lengths it is not possible to obtain objective information from a single autocorrelogram. By constructing peak frequency histograms (Fig. 7), we were able to make some inferences about the spatial organization of MAPs from a set of autocorrelograms. However, variability of curvature and orientation of microtubules in a single micrograph, and differences in magnification between micrographs, tend to blur the structure of the histogram. For these reasons, such histograms have limited value and are most informative when based upon selected scans from a single micrograph.

With our cross-correlation technique, it is possible to assess the significance of the match between individual microdensitometer records and proposed patterns of axial spacing. The corrected correlation index obtained from cross-correlation analysis is an objective measure of the correspondence between the actual arrangement of MAP projections in electron micrographs and a proposed axial pattern of MAP spacing, while the associated confidence level provides a measure of the probability that this correspondence could have occurred by chance. The cross-correlation method does not give absolute information on the patterns of axial spacing. However, used together, the autocorrelation and cross-correlation techniques provide a comprehensive basis for analyzing the spatial organization of MAPs.

We limited our choice of models to single axial repeats and symmetrical superlattices which can be fitted to microtubules with 13 protofilaments, because these models have previously been proposed on the basis of biochemical and morphological data (1, 14, 19, 25, 27). If different models for MAP arrangement are suggested in the future, our microdensitometer–computer correlation analysis could provide a means of assessing their compatibility with the morphological data.

The Arrangement of MAP2

We have developed our techniques using electron micrographs of reconstituted brain microtubules saturated with MAP2. This material was chosen for the following reasons. (*a*) Unlike most microtubules in vivo, it provided homogeneous samples of long, straight microtubules with discrete projections representing a single, well-characterized protein; (*b*) it was readily available; (*c*) identical material has been studied in the past (19); and (*d*) the 12-dimer superlattice model was originally developed from analysis of similar material (1).

We have demonstrated that the match between the pooled MAP2 data and the 12-dimer model is significant at the level $P < 0.02$. While the fit to other models tested was judged to be not significant, the 17-dimer and 24-nm periodic models showed some correspondence with the data (Table II). This is to be expected since both of these models predict some spacings similar to those in the 12-dimer model (see Table I). With our cross-correlation method, the axial spacing of the intrarow bridges in the *Saccinobaculus* axostyle showed a perfect 16-nm axial repeat (Fig. 10 *d*). The lower correlations between the MAP2 data and the 12-dimer superlattice model are not surprising when one examines typical micrographs (Figs. 1 and 2 *a*) and notes how some projections are tilted, the possible missing projections in the lattice, and the presence of electron-dense material lying next to the microtubules which may not be related to MAP2. In fact, taking into account the possible causes of error, we are impressed with how well the MAP2 arrangement correlates with the 12-dimer superlattice model (Table II).

We stress that our method of analysis provides information only on the arrangement of the projection domain of the MAP2 molecule. It does not indicate where the remaining portion of the molecule is located with respect to the surface of the microtubule, nor its mechanism of binding. Therefore, in the microtubules which we have analyzed, we have not concerned ourselves with whether the tubulin dimers are arranged in an A or a B lattice (i.e., a heterologous or a homologous arrangement of tubulin dimers on neighboring protofilaments), or whether they form a discontinuous lattice (2, 3, 24).

It should be noted that, whereas the superlattice models used in the present study are based on microtubules with 13 protofilaments, microtubules synthesized in vitro have been found to contain predominantly 14 protofilaments (3, 19, 22, 24, 30). Kim et al. (19) estimate that up to 95% of their in vitro synthesized microtubules (the same material used in our analysis) contain 14 protofilaments, and it is probable that the microtubules analyzed by Amos (1) were also of this type. Analysis of the tubulin lattice in microtubules with 14 protofilaments indicates that the three-start tubulin monomer helix is conserved, with its pitch angle increased and the dimer lattice discontinuous (22, 24). Therefore, because there is no symmetrical superlattice which fits microtubules with 14 protofilaments, a 12-dimer MAP superlattice may be retained, in a slightly stretched form, in these microtubules.

There is evidence supporting a 12-dimer superlattice arrangement for microtubule projections from other sources. Amos (2) found that the spacings between intermicrotubule bridges of the central spindle of *Barbulanympha*, as measured from electron micrographs, are compatible with a 12-dimer superlattice. Using the cross-correlation technique described here, we have found that the axial spacings of the projections of MAP2-decorated flagellar tubulin (Fig. 14 *c* in reference 4) and of the intermicrotubule bridges in the *Trypanosoma* periplast (18), cold-treated mitotic spindles (18), and the reticulopodia of *Allogromia* (5) are all compatible with a 12-dimer superlattice arrangement, at overall mean confidence levels of 98.3, 99.3, 98.6, and 99.8%,

respectively. In addition, we note that the smallest distances between adjacent interrow bridges in the *Saccinobaculus* axostyle and the intermicrotubule bridges in the perinuclear helix of the chicken spermatid, as measured with a microcomparator by McIntosh (Figs. 2 *a* and 5 *a* in reference 25), are strikingly close to 15 and 22 nm, the basic axial spacings of a 12-dimer superlattice (see Table I).

Although our cross-correlation analysis of MAP2 is most consistent with a 12-dimer superlattice arrangement, 42% of the MAP2 autocorrelograms contained additional peaks which are not accounted for by such an arrangement (Fig. 6 *c*). Also, the mean spacing between data peaks for all 26 MAP2 scans was 18.0 nm, somewhat less than the 20.4-nm mean spacing predicted by the 12-dimer model. These observations are reinforced in the histogram of pooled correlogram peaks (Fig. 7), which shows additional spacings of 11, 25, 65, and 82 nm, none of which is compatible with a 12-dimer superlattice arrangement. These spacings are, however, compatible with a 6-dimer superlattice, which has a superhelix of the same pitch as the 12-dimer model, with twice as many MAP sites along the helix (Table I, Fig. 11). Additional spacings predicted by the 6-dimer model, scaled downward by 4%, are indicated by dots in Fig. 7. However, the results presented in Table II indicate that there is a poor correspondence between MAP2 and a saturated 6-dimer superlattice.

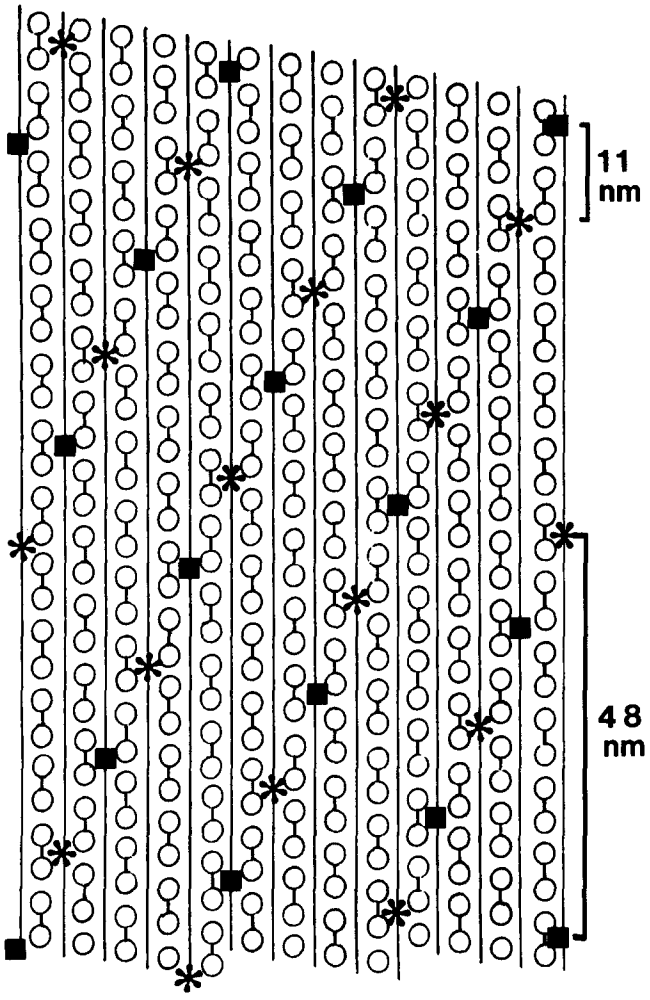

Figure 11. Proposed "saturated 12-dimer, unsaturated 6-dimer" model for the arrangement of MAP2 projections. The squares indicate the high-affinity binding sites of the 12-dimer superlattice; the additional possible low-affinity sites of a 6-dimer superlattice are indicated by asterisks.

A possible explanation for the above observations is that MAP2 preferentially occupies the sites of a 12-dimer superlattice on the surface of the microtubule, but is also able to occupy additional, low-affinity binding sites of a 6-dimer superlattice (Fig. 11). This arrangement would produce some autocorrelogram peaks compatible with 6-dimer spacings but would not result in a high correlation with a 6-dimer model. The degree of saturation of the additional 6-dimer sites would depend upon the extent to which the ratio of MAP2/tubulin was increased above 1:12. Previous estimates of the stoichiometric ratio of MAP2/tubulin in MAP2-saturated microtubules have included 1:4.5 (7), 1:6 (12, 20, 21), 1:7 (R. Vallee, personal communication), 1:9 (19), 1:12 (6), and 1:11–18 (1). The discrepancies could be due to differences in such factors as the source of microtubules, the conditions of reassembly, the amount of saturation with MAP2, or the number of MAP2 breakdown products. However, the various estimates are compatible with the hypothesis that MAP2 associates with the surface of the microtubule in a "saturated 12-dimer, unsaturated 6-dimer" manner. Such a model is also compatible with the findings that brain microtubules in vitro contain two classes of sites which can bind either MAP2 or tau, with different affinities for each MAP (20, 21). Thus, the low-affinity, unsaturated, 6-dimer MAP2 sites could be high-affinity binding sites for tau.

Using the autocorrelation methods described in this paper, we have obtained other evidence of a saturated 12-dimer, unsaturated 6-dimer superlattice arrangement for side-arms and cross-bridges associated with a variety of normal cytoplasmic and spindle microtubules, as well as drug- and cold-treated spindle microtubules (16–18, 32). Therefore, it is possible that such an arrangement may be characteristic of a wide variety of MAPs.

We are deeply indebted to the following people for their generous help during various stages in development of the technique: T. Baker, G. Breckon, A. Cheng, P. Hunter, W. Wilson, and especially R. Joe and G. Kean. We are especially grateful to H. Kim for supplying us with micrographs of MAP2-saturated microtubules and discussing this work. We are extremely grateful to L. Amos for her interest and discussions throughout the course of this work. We thank R. Linck and D. Woodrum for their *Saccinobaculus* micrograph, I. MacDonald and A. Ellis for help in producing the illustrations, J. Carman for critically reading the manuscript, and D. Murphy and *The Journal of Cell Biology* reviewers for their constructive criticism.

The work was supported by grants from the Medical Research Council of New Zealand, the Auckland Medical Research Foundation, and the University of Auckland Research Committee.

Received for publication 30 December 1985, and in revised form 18 April 1986.

References

1. Amos, L. A. 1977. Arrangement of high molecular weight associated proteins on purified mammalian brain microtubules. *J. Cell Biol.* 72:642–654.
2. Amos, L. A. 1979. Structure of microtubules. *In* Microtubules. K. Roberts and J. S. Hyams, editors. Academic Press, Ltd. London. 2–64.
3. Amos, L. A. 1982. Tubulin and associated proteins. *In* Electron Microscopy of Proteins, Vol. 3. J. R. Harris, editor. Academic Press, Ltd. London. 207–250.
4. Binder, L. I., and J. L. Rosenbaum. 1978. The in vitro assembly of flagellar outer doublet tubulin. *J. Cell Biol.* 79:500–515.
5. Bowser, S. S., J. L. Travis, G. Rupp, C. G. Jensen, R. D. Sloboda, and

C. L. Rieder. 1985. A MAP2-like component in reticulopods. *J. Cell Biol.* 101(5, Pt. 2):28a. (Abstr.)

6. Burns, R. G., and K. Islam. 1984. Stoichiometry of microtubule-associated protein (MAP2): tubulin and the localisation of the phosphorylation and cysteine residues along the MAP2 primary sequence. *Eur. J. Biochem.* 141:599–608.

7. Carlier, M.-F., and D. Pantaloni. 1982. Assembly of microtubule protein: role of guanosine di- and triphosphate nucleotides. *Biochemistry.* 21: 1215–1224.

8. Cohen, W. D., D. Bartelt, R. Jaeger, G. Langford, and I. Nemhauser. 1982. The cytoskeletal system of nucleated erythrocytes. I. Composition and function of major elements. *J. Cell Biol.* 93:828–838.

9. Ellisman, M. H., and K. R. Porter. 1980. Microtrabecular structure of the axoplasmic matrix: visualization of cross-linking structures and their distribution. *J. Cell Biol.* 87:464–479.

10. Ensor, D. R., C. G. Jensen, J. A. Fillery, and R. J. K. Baker. 1978. Microdensitometer-computer correlation analysis of ultrastructural periodicity. *Ninth International Congress on Electron Microscopy.* II:32–33.

11. Fuge, H., M. Bastmeyer, and W. Steffen. 1985. A model for chromosome movement based on lateral interaction of spindle microtubules. *J. Theor. Biol.* 115:391–399.

12. Gottlieb, R. A., and D. B. Murphy. 1983. The pattern of MAP-2 binding on microtubules: visual enhancement of MAP attachment sites by antibody labeling and electron microscopy. *J. Ultrastruct. Res.* 85:175–185.

13. Hirokawa, N. 1982. Cross-linker system between neurofilaments, microtubules, and membranous organelles in frog axons revealed by the quick-freeze, deep-etching method. *J. Cell Biol.* 94:129–142.

14. Inoué, S., and H. Ritter. 1975. Dynamics of mitotic spindle organization and function. *In* Molecules and Cell Movement. S. Inoué and R. E. Stephens, editors. Raven Press. New York. 3–30.

15. Jensen, C. G. 1982. Dynamics of spindle microtubule organization: kinetochore fiber microtubules of plant endosperm. *J. Cell Biol.* 92:540–558.

16. Jensen, C. G. 1982. The arrangement of cross-bridges and side-arms in cells of *Haemanthus* endosperm exposed to taxol. *J. Cell Biol.* 95(4, Pt. 2): 335*a*. (Abstr.)

17. Jensen, C. G., and L. C. W. Jensen. 1983. Analysis of cross-bridging between microtubules in cold-treated mitotic cells. *New Zealand J. Sci.* 26:541–542.

18. Jensen, C. G., and B. H. Smaill. 1986. A technique for analysing the spatial organization of microtubular arms and bridges (MAPs). *Ann. NY Acad. Sci.* 466:417–419.

19. Kim, H., L. I. Binder, and J. L. Rosenbaum. 1979. The periodic association of MAP2 with brain microtubules in vitro. *J. Cell Biol.* 80:266–276.

20. Kim, H., C. G. Jensen, and L. I. Rebhun. 1986. The binding of MAP2 and tau on brain microtubules *in vitro*: implications for microtubule structure. *Ann. NY Acad. Sci.* In press.

21. Kim, H., and L. I. Rebhun. 1982. MAP2 and tau competition for binding sites on in vitro assembled brain microtubules. *J. Cell Biol.* 95(2, Pt. 2):349*a*. (Abstr.)

22. Langford, G. M. 1980. Arrangement of subunits in microtubules with 14 protofilaments. *J. Cell Biol.* 87:521–526.

23. Lynn, P. A. 1982. Introduction to the Analysis and Processing of Signals, 2nd edition. Macmillan, London. 222 pp.

24. McEwen, B., and S. J. Edelstein. 1980. Evidence for a mixed lattice in microtubules reassembled *in vitro*. *J. Mol. Biol.* 139:123–145.

25. McIntosh, J. R. 1974. Bridges between microtubules. *J. Cell Biol.* 61:166–187.

26. McIntosh, J. R., E. S. Ogata, and S. C. Landis. 1973. The axostyle of *Saccinobaculus*. *J. Cell Biol.* 56:304–323.

27. Murphy, D. B., and G. G. Borisy. 1975. Association of high-molecular-weight proteins with microtubules and their role in microtubule assembly in vitro. *Proc. Natl. Acad. Sci. USA.* 72:2696–2700.

28. Murphy, D. B., and L. G. Tilney. 1974. The role of microtubules in the movement of pigment granules in teleost melanophores. *J. Cell Biol.* 61:757–779.

29. Olson, G. E., and R. W. Linck. 1977. Observations of the structural components of flagellar axonemes and central pair microtubules from rat sperm. *J. Ultrastruct. Res.* 61:21–43.

30. Pierson, G. B., P. R. Burton, and R. H. Himes. 1978. Alterations in number of protofilaments in microtubules assembled *in vitro*. *J. Cell Biol.* 76:223–228.

31. Pollard, T. D., S. C. Seldon, and P. Maupin. 1984. Interaction of actin filaments with microtubules. *J. Cell Biol.* 99(1, Pt. 2):33s–37s.

32. Reaven, E., C. G. Jensen, M. Spicher, and S. Azhar. 1983. Unique microtubules in luteal cells from superovulated rats. *J. Ultrastruct. Res.* 83:284–295.

33. Sherline, P., Y.-C. Lee, and L. S. Jacobs. 1977. Binding of microtubules to pituitary secretory granules and secretory granule membranes. *J. Cell Biol.* 72:380–389.

34. Sheterline, P. 1978. Localisation of the major high-molecular-weight protein on microtubules in vitro and in cultured cells. *Exp. Cell Res.* 115:460–464.

35. Sloboda, R. D., and K. Dickersin. 1980. Structure and composition of the cytoskeleton of nucleated erythrocytes. I. The presence of microtubule-associated protein 2 in the marginal band. *J. Cell Biol.* 87:170–179.

36. Suprenant, K. A., and W. L. Dentler. 1982. Association between endocrine pancreatic secretory granules and in-vitro–assembled microtubules is dependent upon microtubule-associated proteins. *J. Cell Biol.* 93:164–174.

37. Travis, J. L., and R. D. Allen. 1981. Studies on the motility of the foraminifera. I. Ultrastructure of the reticulopodial network of *Allogromia laticollaris* (Arnold). *J. Cell Biol.* 90:211–221.

38. Vallee, R. 1980. Structure and phosphorylation of microtubule-associated protein 2 (MAP2). *Proc. Natl. Acad. Sci. USA.* 77:3206–3210.

39. Vallee, R. B., G. S. Bloom, and W. E. Theurkauf. 1984. Microtubule-associated proteins: subunits of the cytomatrix. *J. Cell Biol.* 99(1, Pt. 2): 38s–44s.

40. Voter, W. A., and H. P. Erickson. 1982. Electron microscopy of MAP 2 (microtubule-associated protein 2). *J. Ultrastruct. Res.* 80:374–382.

41. Warner, F. D. 1974. The fine structure of the ciliary and flagellar axoneme. *In* Cilia and Flagella. M. A. Sleigh, editor. Academic Press, Ltd. London. 11–37.

42. Woodrum, D. T., and R. W. Linck. 1980. Structural basis of motility in the microtubular axostyle: implications for cytoplasmic microtubule structure and function. *J. Cell Biol.* 87:404–414.

43. Woody, R. W., G. C. K. Roberts, D. C. Clark, and P. M. Bayley. 1982. ^{1}H NMR evidence for flexibility in microtubule-associated proteins and microtubule protein oligomers. *FEBS (Fed. Eur. Biochem. Soc.) Lett.* 141:181–184.

44. Zingsheim, H.-P., W. Herzog, and K. Weber. 1979. Differences in surface morphology of microtubules reconstituted from pure brain tubulin using two different microtubule-associated proteins: the high molecular weight MAP 2 proteins and tau proteins. *Eur. J. Cell Biol.* 19:175–183.